THE JOURNAL OF PHYSICAL CHEMISTRY A

Article

Cite This: J. Phys. Chem. A 2019, 123, 2559−2569

pubs.acs.org/JPCA

CH Stretch Activation of CH_3CHOO: Deep Tunneling to Hydroxyl Radical Products

Published as part of The Journal of Physical Chemistry virtual special issue "Hanna Reisler Festschrift".

Victoria P. Barber,[†] Shubhrangshu Pandit,[†] Vincent J. Esposito,[†] Anne B. McCoy,[‡] and Marsha I. Lester*,[†]

[†]Department of Chemistry, University of Pennsylvania, Philadelphia, Pennsylvania 19104-6323, United States

[‡]Department of Chemistry, University of Washington, Seattle, Washington 98195-1700, United States

Supporting Information

ABSTRACT: Alkene ozonolysis, an important source of hydroxyl (OH) radicals in the Earth's troposphere, proceeds through unimolecular decay of Criegee intermediates. In this work, infrared activation of the methyl-substituted Criegee intermediate, *syn*-CH_3CHOO, in the CH stretch fundamental region (2850−3150 cm^{-1}) is shown to result in unimolecular decay to OH radical products. These excitation energies correspond to only half of the transition state barrier height, and thus the resultant 1,4 H atom transfer that leads to OH products occurs exclusively by quantum mechanical tunneling. Infrared action spectra recorded with UV laser-induced fluorescence detection of the OH products reveal the four CH stretch fundamentals and CO stretch overtone predicted to have strong transition strength. The vibrational band origins, relative intensities, and transition types derived from rotational band contour analyses are in good accord with theory. Distinctly different Lorentzian line broadening of the observed features is attributed to mode-specific anharmonic couplings predicted theoretically between spectroscopically bright and nearby dark states. The measured OH product state distribution shows a strong λ-doublet preference arising from pπ orbital alignment, which is indicative of the vinyl hydroperoxide intermediate along the reaction pathway. The unimolecular decay of *syn*-CH_3CHOO at ca. 3000 cm^{-1} is predicted to be quite slow (ca. 10^5 s^{-1}) using statistical Rice-Ramsperger-Kassel-Marcus theory with tunneling and much slower than observed at higher energies.

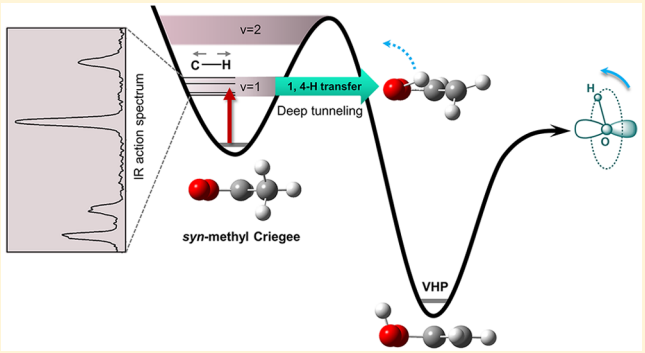

1. INTRODUCTION

Hydroxyl (OH) radicals are key atmospheric oxidants that initiate the breakdown of trace species in the Earth's lower atmosphere. Alkene ozonolysis is an important nonphotolytic source of OH radicals. Both atmospheric modeling and field studies suggest that alkene ozonolysis is the main source of OH radicals at nighttime and a significant source (up to 24%) during the daytime.[1−5] Additionally, alkene ozonolysis is of particular significance as a source of OH radicals in wintertime, when low UV light levels reduce photolytic OH production.[1] In boreal forests and terrestrial rainforests, where alkene concentrations are high, up to 13% of total OH radicals are predicted to be formed from alkene ozonolysis.[5]

Alkene ozonolysis proceeds by addition of ozone (O_3) across the C═C double bond to form a primary ozonide (POZ), which rapidly decomposes to a carbonyl and a carbonyl oxide species, the latter known as a Criegee intermediate, in a highly exothermic process.[6] Upon formation in the atmosphere, internally excited Criegee intermediates may undergo prompt unimolecular decay to produce OH radicals and other products. Alternatively, the Criegee intermediates may be collisionally stabilized and undergo thermal unimolecular decay[7−9] or bimolecular reaction with other atmospheric species including water vapor and SO_2,[10−15] which may result in atmospheric aerosol formation.[16,17]

The atmospheric fate of the Criegee intermediates depends on both their substituents and conformational forms. For *syn*-alkyl-substituted Criegee intermediates, such as *syn*-CH_3CHOO, unimolecular decay proceeds via 1,4 H atom transfer, in which an α-H atom on the *syn*-alkyl group transfers to the terminal oxygen atom via a five-membered cyclic transition state (TS), to form vinyl hydroperoxide (VHP).[8,18−20] For *syn*-CH_3CHOO, the TS barrier has been predicted to be 17.05 kcal mol^{-1} (5968 cm^{-1}).[21] Subsequent O−O bond cleavage produces OH and vinoxy radicals, as shown in Figure 1.[8,18−20] For *syn*-CH_3CHOO and $(CH_3)_2COO$, unimolecular decay to OH via this mechanism is predicted to be the dominant atmospheric loss proc-

Received: December 21, 2018
Revised: February 15, 2019
Published: March 6, 2019

DOI: 10.1021/acs.jpca.8b12324
J. Phys. Chem. A 2019, 123, 2559−2569

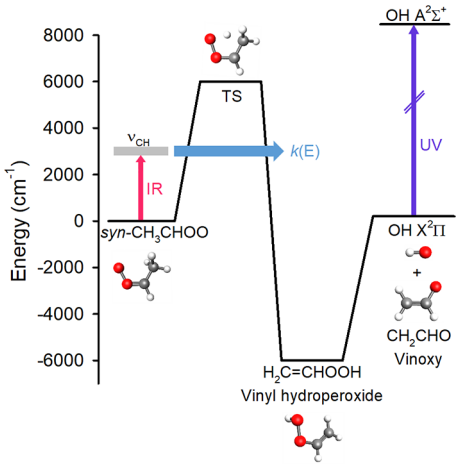

Figure 1. Reaction coordinate for the unimolecular decay of *syn*-CH_3CHOO. The unimolecular reaction involves a 1,4 H atom transfer to vinyl hydroperoxide ($H_2C{=}CHOOH$) via a transition state (TS), followed by dissociation to produce OH and vinoxy radical products. Experimentally, IR radiation is used to excite *syn*-CH_3CHOO in the ν_{CH} region (~3000 cm^{-1}), which corresponds to approximately half of the TS barrier to reaction. The OH radical products are state-selectively detected via UV LIF.

ess.[9,21−23] For Criegee intermediates lacking an alkyl α-H atom, such as CH_2OO, this pathway is unavailable. Unimolecular decay may still occur, but it will proceed by alternative reaction mechanisms and lead to numerous products.[24−27]

Recently, this laboratory performed energy-dependent rate measurements for the unimolecular decay to OH products of a series of *syn*-alkyl-substituted Criegee intermediates, including *syn*-CH_3CHOO.[21−23,28−31] In these studies, IR radiation is used to vibrationally activate the Criegee intermediates, which provides sufficient energy to surmount or tunnel through the TS barrier. A variably delayed UV laser pulse then probes the resulting OH products by laser-induced fluorescence (LIF). Initially, these experiments were undertaken at energies in the vicinity of the TS barrier (ca. 6000 cm^{-1}), which are accessed via IR excitation of vibrational transitions with two quanta of CH stretch ($2\nu_{CH}$). For *syn*-CH_3CHOO, the unimolecular decay rates are on the order of 10^8 s^{-1} in this energy regime. The experimentally observed OH appearance rates are in near quantitative agreement with complementary microcanonical statistical Rice-Ramsperger-Kassel-Marcus (RRKM) rate calculations incorporating quantum mechanical tunneling.[21]

Subsequently, OH radical products were observed following IR activation of *syn*-CH_3CHOO and $(CH_3)_2COO$ at energies significantly below the TS barrier (ca. 4000 cm^{-1}). In these experiments, IR excitation accesses combination bands involving one quantum of CH stretch and one quantum of another, lower frequency vibrational mode ($\nu_{CH} + \nu_i$). At these energies, OH production from *syn*-CH_3CHOO occurs at a 100-fold slower rate (10^6 s^{-1}). Again, the experimentally observed OH appearance rates are in good agreement with microcanonical RRKM calculations incorporating tunneling. At energies nearly 2000 cm^{-1} below the TS barrier, the reaction occurs exclusively via quantum mechanical tunneling.[22,23]

The importance of tunneling in the unimolecular decay of Criegee intermediates has been further verified by energy-dependent rate measurements of a partially deuterated isotopologue of *syn*-CH_3CHOO, *syn*-CD_3CHOO. In this experiment, *syn*-CD_3CHOO is vibrationally activated with two quanta of CH stretch ($2\nu_{CH}$), initiating a 1,4 D atom transfer and resulting in OD products, which are detected by LIF. The heavier deuterium atom slows the tunneling rate and results in a significant energy-dependent kinetic isotope effect (KIE) of ca. 10 at ca. 6000 cm^{-1}.[29]

The experimentally verified microcanonical rate calculations have been extended to predict thermal unimolecular decay rates $k(T)$ in the high-pressure limit under atmospheric conditions. The thermal decay rate for *syn*-CH_3CHOO at 298 K is predicted to be 166 s^{-1} and agrees with subsequent theoretical predictions.[22,32,33] For the selectively deuterated *syn*-CD_3CHOO, the predicted thermal rate at 298 K is only 3 s^{-1}.[29] The large thermal KIE provides further evidence of the importance of tunneling in the unimolecular decay of Criegee intermediates under atmospheric conditions.

For thermalized Criegee intermediates under atmospheric conditions, $k(T)$ can be represented as a Boltzmann weighted average of the microcanonical rates $k(E)$ over a range of energies:[34]

$$k(T) \propto \int k(E)N(E)\exp\left(-\frac{E}{k_B T}\right) dE$$

Here, $N(E)$ is the density of vibrational states of the Criegee intermediate, and $\exp(-E/k_BT)$ is the Boltzmann factor representing the population distribution of the Criegee intermediates. While the Boltzmann factor decreases exponentially with energy, both the microcanonical rate $k(E)$ and the density of states $N(E)$ increase rapidly with energy. The product of the three terms of the integrand, as shown in Figure 2, reflects the relative contribution of $k(E)$ at different energies to the thermal rate $k(T)$. At 300 K, $k(T)$ has large contributions from energies at ~3000 cm^{-1}, far below the TS barrier, further illustrating the importance of tunneling under thermal decay conditions.[22] By comparison, for $(CH_3)_2COO$, $k(T)$ had its largest contribution from slightly higher energies at ca. 4200 cm^{-1}.[23]

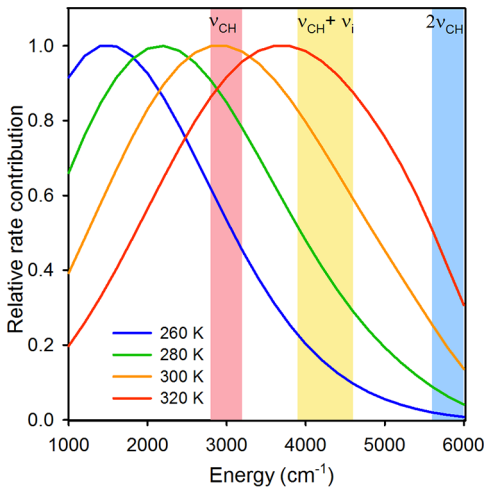

Figure 2. Relative contributions of microcanonical rate coefficients $k(E)$ to the thermal decay rate coefficient $k(T)$ for *syn*-CH_3CHOO at atmospherically relevant temperatures T = 260−320 K. The shaded blocks represent energy regions in which unimolecular decay from *syn*-CH_3CHOO to OH has been experimentally observed: $2\nu_{CH}$ (blue),[21] $\nu_{CH} + \nu_i$ (yellow),[22] and ν_{CH} (red, present work).

DOI: 10.1021/acs.jpca.8b12324
J. Phys. Chem. A 2019, 123, 2559−2569

In this work, we demonstrate the production of OH radicals following IR activation of *syn*-CH_3CHOO in the CH stretch fundamental region. We report an IR action spectrum of *syn*-CH_3CHOO in the 2850−3150 cm^{-1} region with detection of OH products. Experimental vibrational frequencies and transition types are compared with complementary theoretical calculations of *syn*-CH_3CHOO. Vibrational coupling calculations are performed to provide further insight on observed spectral features and the first stage of intramolecular vibrational dynamics in this energy regime. Excitation at ca. 3000 cm^{-1}, approximately half of the TS barrier height, is shown to result in significantly slower unimolecular decay than observed at higher energies. Finally, a pronounced orbital alignment of the OH products is observed that reflects the reaction pathway leading to dissociation of *syn*-CH_3CHOO.

2. METHODS

The *syn*-CH_3CHOO Criegee intermediate is generated in a pulsed supersonic expansion as described previously.[20−22,35] Briefly, the 1,1-diiodoethane precursor is entrained in 10% O_2/Ar carrier gas at a pressure of 20 psi and introduced into a quartz capillary reactor tube via a pulsed valve, where it is photolyzed by the 248 nm output of a KrF excimer laser (Coherent Compex Pro 50, 20 Hz, 40 mJ/pulse), which is loosely focused along the length of the capillary tube using a cylindrical lens. The monoiodo radical reacts with O_2 to produce the *syn*-CH_3CHOO Criegee intermediate, which is collisionally stabilized and cooled to a rotational temperature of 10 K in a supersonic expansion into vacuum. Approximately 1 cm downstream, the gas mixture is intersected in the collision-free region by counter-propagating and spatially overlapped IR and UV laser beams. The IR pump and UV probe are loosely focused to beam diameters of ∼1 and 3 mm, respectively.

The tunable IR radiation excites the *syn*-CH_3CHOO in the CH stretch fundamental (ν_{CH}) region, initiating unimolecular decay, and the UV laser probes the OH $X^2\Pi_{3/2}$ (v = 0) product by LIF. The IR radiation (∼11 mJ/pulse, 7 ns full width at half-maximum (fwhm)) is the idler output of an infrared optical parametric oscillator/amplifier (OPO/OPA, LaserVision) pumped by the 1064 nm output of an injection-seeded Nd:YAG laser (Continuum Surelite EX, 10 Hz, 680 mJ/pulse; NP photonics Rock Fiber Laser Seeder). The Nd:YAG pump laser is operated in seeded and unseeded modes, giving rise to OPO/OPA bandwidths of 0.15 and 0.9 cm^{-1}, respectively, for higher- and lower-resolution scans. The UV probe (∼3.5 mJ/pulse, 6 ns fwhm) is the frequency-doubled output of a Nd:YAG (Continuum Precision II 7020, 532 nm, 20 Hz) pumped dye laser (ND6000, Rhodamine 590 dye), which utilizes an autotracker (Inrad Autotracker III) with a KDP doubling crystal. The resultant OH $X^2\Pi_{3/2}$ (v = 0, *N*) radicals are probed on Q_1 and P_1 lines of the $A^2\Sigma^+-X^2\Pi_{3/2}$ (1,0) transition under saturated LIF conditions.[36] Active background subtraction (IR on − IR off) is implemented to remove background OH, which arises from unimolecular decay of energized Criegee intermediates in the capillary tube and subsequent cooling in the free jet expansion. The OH A-X (1,0) $Q_1(3)$ line gives the best signal-to-background ratio in the IR action spectra. The fluorescence emitted on the OH $A^2\Sigma^+-X^2\Pi_{3/2}$ (1,1) band is collected with a gated photomultiplier tube (Electron Tubes 9812QB). The output signal is preamplified and displayed on a digital storage oscilloscope (LeCroy WaveRunner 44Xi) interfaced with a computer for processing.

A computed anharmonic IR absorption spectrum for *syn*-CH_3CHOO is evaluated at the B2PLYPD3/cc-pVTZ level of theory using vibrational second-order perturbation theory (VPT2) as implemented in the Gaussian 16 program suite.[37] Intensities and transition types calculated before and after variational correction to the VPT2 wave function are reported in Table S1.

RRKM theory is also utilized to predict the statistical, energy-dependent unimolecular dissociation rate $k(E)$ of *syn*-CH_3CHOO as described previously.[21,22] Tunneling is incorporated using an SCTST model[38−43] as implemented in Multiwell.[44−46] The energy-dependent microcanonical unimolecular dissociation rate constant $k(E)$ at a given energy E is given by[47]

$$k(E) = \frac{\sigma_{\text{eff}}}{\sigma_{\text{eff}}^*}\frac{G^{\ddagger}(E - E_0)}{hN(E)}$$

where E_0 is the TS energy barrier to reaction, $G^{\ddagger}(E - E_0)$ is the sum of states at the TS, $N(E)$ is the density of states of the Criegee intermediate, and h is Planck's constant. The effective symmetry numbers σ_{eff} for the reactants and σ_{eff}^* for the TS are 1 and 1/2, respectively. The methyl torsion is treated as a one-dimensional hindered rotor. Previously, the energies of *syn*-CH_3CHOO Criegee intermediate, the TS barrier, and the VHP necessary for the kinetic rate calculations were obtained using high-level electronic structure theory [CCSD(T, full)/CBS with corrections] with anharmonic zero-point energy corrections.[21] The rovibronic properties of the *syn*-CH_3CHOO Criegee intermediate and the TS are calculated at the B2PLYPD3/cc-pVTZ level of theory as implemented in Gaussian 16, and they are given in Tables S2 and S3.

3. RESULTS

The *syn*-CH_3CHOO Criegee intermediate is vibrationally activated at ca. 3000 cm^{-1} via IR excitation in the CH stretch fundamental region. This energy is approximately half of the TS barrier associated with the 1,4 H atom transfer that leads to OH products. Vibrationally activated *syn*-CH_3CHOO undergoes unimolecular decay to OH via quantum mechanical tunneling. The OH radical products are detected by subsequent UV excitation and LIF. In this work, two types of experiments are performed: (1) The IR pump laser is scanned at a fixed IR-UV time delay to generate an IR action spectrum of jet-cooled *syn*-CH_3CHOO Criegee intermediates. (2) Following IR excitation of *syn*-CH_3CHOO at a known feature in the IR action spectrum, the UV probe wavelength is varied to measure the product state distribution of the resulting OH radicals.

3.1. IR Action Spectrum. The experimental IR action spectrum of *syn*-CH_3CHOO with detection of OH products is obtained by scanning the IR pump laser in the CH stretch fundamental region at a fixed IR-UV time delay of 1200 ns. The OH products, which result exclusively from tunneling through the TS barrier, are detected by LIF on the OH $A^2\Sigma^+-X^2\Pi_{3/2}$ $Q_1(3)$ transition. A low-resolution (0.9 cm^{-1}) scan of the IR action spectrum reveals four strong features, as shown in Figure 3 (top panel). Following initial survey scans, subsequent high-resolution (0.15 cm^{-1}) scans of each feature were performed to reveal their rotational band contours, as shown in Figure 3 (middle panel).

DOI: 10.1021/acs.jpca.8b12324
J. Phys. Chem. A 2019, 123, 2559−2569

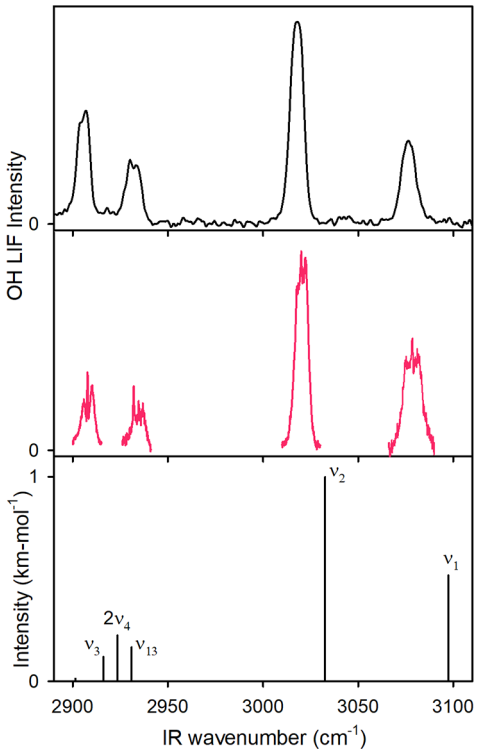

Figure 3. (top) Experimental IR action spectrum at low-IR resolution (OPO bandwidth of 0.9 cm^{-1}) observed for the *syn*-CH_3CHOO Criegee intermediate in the CH stretch fundamental (ν_{CH}) region from 2850 to 3150 cm^{-1} with UV LIF detection of OH products at an IR-UV time delay of 1200 ns. (middle) Experimental IR action spectrum of the prominent spectral features recorded at higher-IR resolution (OPO bandwidth of 0.15 cm^{-1}) at the same time delay. (bottom) Computed anharmonic IR spectrum (VPT2) at the B2PLYPD3/cc-pVTZ level of theory. CH stretch fundamentals (ν_1, ν_2, ν_3, and ν_{13}) and a CO stretch overtone ($2\nu_4$) are predicted in this energy region.

IR action spectroscopy differs from IR absorption spectroscopy, in that IR activation of the spectral carrier must lead to OH products in order for a signal to be observed. As a result, the observed intensities in the IR action spectrum depend not only on the intrinsic IR transition strengths (as in theoretically predicted IR spectra or direct IR absorption measurements) but also on the OH product yield at a specific time delay and, by extension, on the OH appearance rate, as further discussed in Section 4. Additionally, because IR activation must lead to OH production to observe signal, it is unlikely that *anti*-CH_3CHOO contributes to the observed IR action spectrum. The unimolecular decay of *anti*-CH_3CHOO is predicted to proceed via a 1,3 ring-closure mechanism to dioxirane with a high calculated TS barrier of 15.3−15.7 kcal mol^{-1} (5355−5495 cm^{-1}),[24,33] followed by decay to many products including a small yield of OH.[48] This pathway involves a heavy-atom motion, does not proceed by quantum mechanical tunneling, and therefore will not be accessible at the energy range utilized in this work.[25]

The IR absorption spectrum in the ν_{CH} region is predicted theoretically at the B2PLYPD3/cc-pVTZ level of theory using VPT2 with variational correction to the VPT2 wave function and is also shown in Figure 3 (bottom panel). The predicted spectrum exhibits five strong IR transitions in this energy region. Four of these are the fundamentals in the four CH stretches (ν_1, ν_2, ν_3, ν_{13}). Of these, three involve A′ vibrations and are predicted to be *a*-type (ν_2) or mixed *a*/*b*-type (ν_1 and ν_3) transitions, where the transition dipole moment is in the plane of the molecule. Only one, ν_{13}, is predicted to be a *c*-type transition, involving an A″ vibration, in which the transition dipole moment is perpendicular to the molecular plane. The other strong transition arises from two quanta of CO stretch ($2\nu_4$), and it is predicted to be *a*-type. There are several other two-quanta transitions predicted in this energy regime, arising from either overtones or combination bands of other lower-frequency modes. However, on the basis of calculations at this level of theory, none of these are predicted to have appreciable IR intensity. Additional details on calculated transitions are given in Table S1.

3.2. Rotational Band Contour Analysis and Vibrational Assignments. Each of the features observed in the IR action spectrum display rotational structure, although some features have more distinctive rotational band contours than others. Expanded views of each feature, along with rotational band contour fits, are shown in Figures 4, 5, and S1. In all cases, the simulations are based on experimentally determined rotational constants, which are assumed to be unchanged upon vibrational excitation.[49] The simulations include a Gaussian line width of 0.15 cm^{-1} associated with the IR laser bandwidth; a simulation at the laser line width is also shown in each figure for comparison. The remaining parameters of the spectral simulations, including band origins, transition type, homogeneous (Lorentzian) broadening, and rotational temperature, are determined via a least-squares fit using the PGOPHER spectral simulation program.[50] The fit parameters for each feature are given in Table S4.

The most defined rotational band contour is observed for the feature at 2907.8 cm^{-1}, shown in Figure 4a. The experimental feature is fit to an *a*/*b* (0.60/0.40) transition type with a rotational temperature of ca. 10 K and a

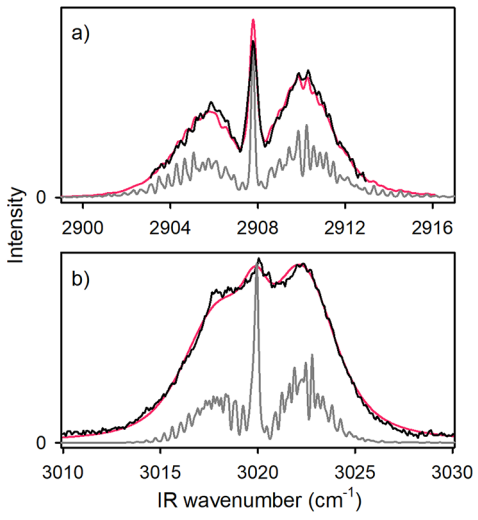

Figure 4. Expanded views of the spectral features (black) at (a) 2907.8 and (b) 3020.0 cm^{-1} in the IR action spectrum of jet-cooled *syn*-CH_3CHOO with superimposed rotational contour simulations (red) using experimental rotational constants.[49] These features are assigned to the (a) ν_3 methyl in-plane CH stretch and (b) ν_2 methyl in-plane CH stretch. Spectral simulations indicate a rotational temperature of ∼10 K, Lorentzian line widths of (a) 0.31 and (b) 1.4 cm^{-1}, and *a*/*b*-transition types of (a) 0.60/0.40 and (b) 0.56/0.44. Rotational band simulations at the OPO bandwidth of 0.15 cm^{-1} (gray) are included for comparison.

DOI: 10.1021/acs.jpca.8b12324
J. Phys. Chem. A 2019, 123, 2559−2569

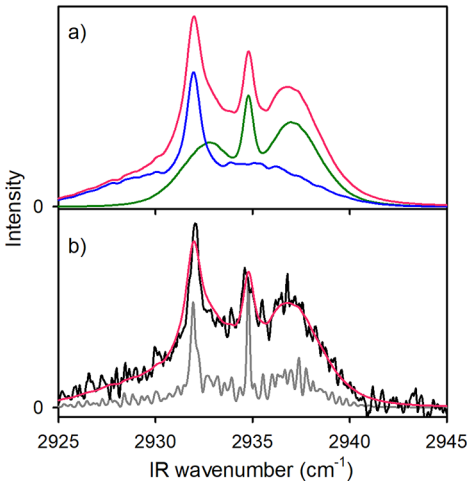

Figure 5. (lower) Expanded view of the feature centered at ca. 2935 cm^{-1} (black) in the experimental IR action spectrum of *syn*-CH_3CHOO. The superimposed rotational contour fit (red) involves two overlapping transitions with band origins at 2932.0 cm^{-1} (*c*-type) and 2934.8 cm^{-1} (*a*/*b*-type). The simulation utilizes experimental rotational constants,[49] a Lorentzian line width of 0.66 cm^{-1}, and a rotational temperature of ∼10 K. A simulation at the laser bandwidth (gray) is included for comparison. (upper) Simulated rotational band contours for the two contributing transitions: a *c*-type transition at 2932.0 cm^{-1} (blue) assigned to the ν_{13} methyl out-of-plane asymmetric CH stretch and an *a*/*b*-type transition at 2934.8 cm^{-1} (green) assigned to the CO stretch overtone $2\nu_4$. The sum of the two simulations (red) is shown in both panels.

homogeneous (Lorentzian) line broadening of 0.31 cm^{-1}. This feature is assigned to the ν_3 methyl in-plane CH stretch, predicted at 2916.2 cm^{-1}, with a calculated *a*/*b* (0.30/0.70) transition type. Differences between the experimental and calculated transition types for this and other features will be discussed in Section 4.

A less-distinctive rotational band contour is seen for the strongest experimentally observed feature at 3020.0 cm^{-1}, shown in Figure 4b. Here, the experimental feature is fit to an *a*/*b* (0.56/0.44) transition type, again with a rotational temperature of ca. 10 K. Interestingly, this feature exhibits a significantly greater Lorentzian broadening of 1.4 cm^{-1}, which may arise from vibrational couplings discussed in Section 4. This feature is assigned to the ν_2 methyl in-plane CH stretch, predicted at 3032.6 cm^{-1}, which is calculated to be an *a*-type transition.

We also observe a feature at ca. 3078 cm^{-1}. The OPO/OPA system exhibits a ca. 20% variation in power when scanned across this feature, because the OPO crystals are near normal incidence. As a result, the experimental spectrum is linearly power-corrected. The frequency of this feature matches reasonably well with the strong carbonyl oxide CH stretch (ν_1) predicted at 3097.4 cm^{-1}. However, as shown in Figure 3 and Figure S1, this feature is unique in that its overall breadth is significantly greater than the other features observed in this region, suggesting that there may be another state coupled to ν_1. When the whole feature is fit to a rotational band contour, we find a surprisingly high rotational temperature of ca. 20 K compared to that observed for other *syn*-CH_3CHOO features in the CH stretch fundamental (ν_{CH}), combination band (ν_{CH} + ν_i), and overtone ($2\nu_{CH}$) regions of ca. 10 K. Because the experimental conditions are the same in this and prior studies,[21,22] it is unlikely that the rotational temperature of this feature would be so different. A more plausible explanation is that an adjacent, overlapping lower intensity transition (see Figure S1) gains strength by coupling to ν_1 (see Section 4.1) and causes the feature to appear broader (fwhm of 11.5 cm^{-1} as opposed to a fwhm of ca. 8 cm^{-1} for a typical *a*/*b*-type feature at 10 K). If we fit only the lower-frequency half of the feature to a rotational band contour, we find a more reasonable rotational temperature of 9.1 K, and thus we slightly favor this option. We note that, in both cases, the fitted regions of the 3078 cm^{-1} feature are well-represented as mixed *a*/*b*-type transition, consistent with the theoretically predicted ν_1 transition type, and with a relatively large Lorentzian line width of ca. 2 cm^{-1}.

Finally, we observe a feature centered at ca. 2935 cm^{-1}, shown in Figure 5. The overall shape of this feature is not consistent with a single *a*/*b*- or *c*-type transition; it exhibits two quite sharp peaks and one broader peak. However, the feature is well-represented by a fit to two overlapping transitions. One is an *a*/*b* (0.77/0.23) type of transition with a band origin at 2934.8 cm^{-1}. The other is a *c*-type transition with a band origin at 2932.0 cm^{-1}. The overall contour is again simulated with a rotational temperature of ca. 10 K. Here, the Lorentzian line width is 0.66 cm^{-1}. However, this is likely only an estimate of the homogeneous broadening, which is assumed to be equal for the two overlapping features. The upper panel of Figure 5 shows the two overlapping rotational band contours and the sum deduced in the spectral simulation. The experimental feature is tentatively assigned to the overlapping $2\nu_4$ (*a*-type) CO stretch overtone and ν_{13} (*c*-type) methyl out-of-plane asymmetric CH stretch, predicted at 2923.5 and 2930.9 cm^{-1}, respectively. Because of the different symmetries of the $2\nu_4$ (A′) and the ν_{13} (A″) states, there is no coupling between them, and the feature can be represented as a sum of two distinct, non-interacting, but overlapping bands.

3.3. OH Product State Distributions. The rotational state distributions of the nascent OH $X^2\Pi_{3/2}$ (v = 0, *N*) products are also determined following IR activation of *syn*-CH_3CHOO on the ν_2 and ν_3 transitions at 3020.0 and 2907.8 cm^{-1}, respectively. The UV probe laser power is sufficient to fully saturate the OH A-X (1,0) transitions. As a result, the LIF intensities measured on OH A-X (1,0) Q_1 and P_1 lines can be directly related to the relative population of the OH $X^2\Pi_{3/2}$ (v = 0, *N*) rotational levels utilizing a degeneracy term, rather than the Hönl−London factors required in the unsaturated case.[36,51] (We were unable to eliminate a small contribution from overlapping satellite lines.) The nascent OH $X^2\Pi_{3/2}$ (v = 0, *N*) rotational distribution obtained by probing A-X (1,0) Q_1 and P_1 lines following *syn*-CH_3CHOO ν_2 excitation is shown in Figure 6; a similar distribution is observed upon ν_3 excitation. In both cases, the OH $X^2\Pi_{3/2}$ (v = 0, *N*) product distribution peaks at *N* = 2−3 and falls off to higher *N*. (Note that the population of *N* = 1 products cannot be determined due to its very large background from OH generated in the source and cooled in the expansion.) Similar OH $X^2\Pi_{3/2}$ (v = 0, *N*) distributions are obtained upon IR excitation of *syn*-CH_3CHOO in the combination (ν_{CH} + ν_i) and CH stretch overtone ($2\nu_{CH}$) regions.[20]

Additional information can be obtained by comparison of the population distributions derived from Q_1 and P_1 lines. Each of the OH rotational levels is split into two closely spaced λ-doublet components, arising from the interaction between the electronic angular momentum and rotational angular momentum in OH.[52−54] P_1 lines monitor the Π(A′) λ-doublet and Q_1

DOI: 10.1021/acs.jpca.8b12324
J. Phys. Chem. A 2019, 123, 2559−2569

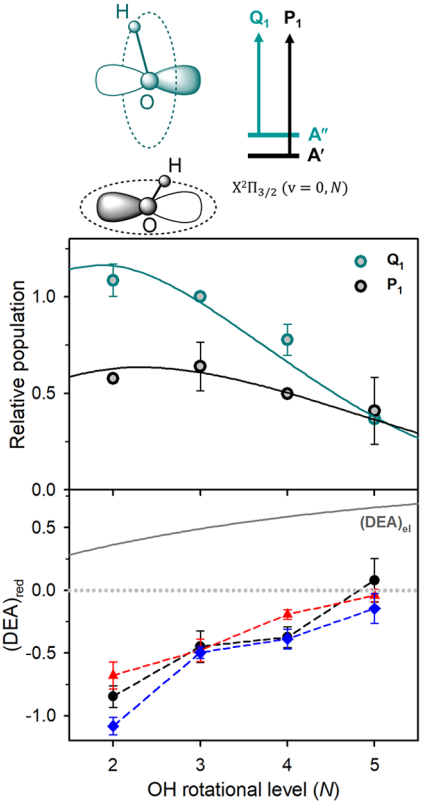

Figure 6. (upper) Population of OH $X^2\Pi_{3/2}$ (v = 0, N) product rotational levels derived from saturated LIF measurements on the OH $A^2\Sigma^+ - X^2\Pi_{3/2}$ (1,0) transition following IR excitation of *syn*-CH_3CHOO in the CH stretch fundamental (ν_{CH}) region at 3020 cm^{-1}. OH Q_1 lines (cyan) preferentially probe $\Pi(A'')$ λ-doublet levels, while OH P_1 lines (black) preferentially probe $\Pi(A')$ λ-doublet levels (top scheme). The smooth curves through the data points represent a fit of the observed OH product rotational distribution to a Boltzmann distribution with rotational temperature (T_{rot}) of 365 K for Q_1 lines (cyan) and 535 K for P_1 lines (black) for N = 2−5 levels. (lower) The reduced degree of electron alignment $(DEA)_{red}$ deduced for OH $X^2\Pi_{3/2}$ (v = 0, N) products following IR excitation of *syn*-CH_3CHOO on a CH stretch fundamental (ν_{CH}) at 3020 cm^{-1} (black), combination band at 4107.8 cm^{-1} (red), and CH stretch overtone ($2\nu_{CH}$) at 6082.8 cm^{-1} (blue).[20] The purely electronic component of the electron alignment $(DEA)_{el}$ (gray) in low OH rotational levels is taken into account in the analysis. Half-filled $p\pi$ orbital alignment of the OH product perpendicular to the OH rotation plane (cyan) is designated as $(DEA)_{red} = -1$, alignment in the OH rotation plane (black) results in $(DEA)_{red} = +1$, and no alignment gives $(DEA)_{red} = 0$. (See Section 4.3.)

lines probe the $\Pi(A'')$ λ-doublet.[52,55] The $\Pi(A')$ or $\Pi(A'')$ notation refers to whether the electronic wave function is symmetric or antisymmetric with respect to reflection in the OH plane of rotation.[52,56] As shown in Figure 6, the $\Pi(A'')$ λ-doublet is favored over the $\Pi(A')$ level for N = 2−4, indicating a λ-doublet population inversion.[52] This preferential population of the upper $\Pi(A'')$ λ-doublet of the OH products is observed upon IR activation of *syn*-CH_3CHOO in three energy regimes: CH fundamental (ν_{CH}), combination ($\nu_{CH} + \nu_i$), and overtone ($2\nu_{CH}$) regions. This preference provides dynamical information, which is explored in Section 4.3.

4. DISCUSSION

In this study, we show that unimolecular decay of *syn*-CH_3CHOO can be driven by IR excitation at ca. 3000 cm^{-1}, which corresponds to an energy of approximately half of the calculated TS barrier (5968 cm^{-1}). The discussion focuses on the mode-specific couplings between the optically bright and nearby dark states and on subsequent intramolecular vibrational redistribution among a sparse density of states (ca. 5 states/cm^{-1}) that leads to reaction. Statistical RRKM rates including quantum mechanical tunneling are evaluated for unimolecular decay of *syn*-CH_3CHOO in this deep tunneling regime and compared with an estimate of the OH appearance rate based on experiment. Lastly, the $p\pi$ orbital alignment of the OH products is attributed to a dynamical effect arising from geometric changes along the reaction coordinate leading to products.

4.1. IR Action Spectroscopy and Vibrational Couplings. The predicted IR absorption spectrum of *syn*-CH_3CHOO in the CH stretch fundamental region (2850 to 3150 cm^{-1}) exhibits five strong transitions. Each of these transitions is observed and assigned in the experimentally observed IR action spectrum. The overall agreement between the experimental and theoretically predicted energies of the transitions is quite good, confirming the identity of *syn*-CH_3CHOO as the spectral carrier.

There are several experimental observables that provide insight into the anharmonic couplings between vibrational modes in this energy region. For example, the methyl out-of-plane symmetric CH stretch, ν_3, which exhibits the most distinctive experimentally observed rotational band contour, exhibits an experimental transition type of a/b = 0.60/0.40. This agrees much better with the calculated deperturbed anharmonic transition type (a/b = 0.74/0.26) than that calculated after variational correction to the VPT2 wave function (a/b = 0.30/0.70). This difference between the two calculated transition types is due to the inclusion of mixing between the first overtone of the CO stretch ($2\nu_4$) and ν_3 in the variationally corrected calculation. We note that the experimentally observed energy separation between ν_3 and $2\nu_4$ is significantly larger than that predicted at this level of theory (27 vs 7 cm^{-1}, respectively). It is therefore likely that the calculation overestimates the degree of mixing of these two vibrational states (ν_3 and $2\nu_4$), leading to a calculated transition type that differs from experiment when the $\nu_3/2\nu_4$ coupling is included.

We also observe marked differences in Lorentzian line broadening among different features (see Table S4), which is likely related to mode-specific coupling that initiates intramolecular vibrational energy redistribution (IVR). Specifically, the methyl out-of-plane symmetric CH stretch fundamental (ν_3) exhibits the smallest Lorentzian broadening of only 0.31 ± 0.01 cm^{-1}, while the carbonyl oxide CH stretch (ν_1) and the methyl in-plane CH stretch (ν_2) show significantly larger Lorentzian line broadenings of 1.9 ± 0.1 and 1.41 ± 0.03 cm^{-1}, respectively. The first overtone of the CO stretch ($2\nu_4$) exhibits an intermediate broadening of 0.66 ± 0.02 cm^{-1}. However, because of the overlap of $2\nu_4$ and the out-of-plane, asymmetric CH stretch (ν_{13}), the determination of the broadening of this feature is less certain. We considered, but cannot completely exclude, the possibility of IR power broadening of the rotational band contours, even though we observe a linear power dependence (Figure S2). Nevertheless,

DOI: 10.1021/acs.jpca.8b12324
J. Phys. Chem. A 2019, 123, 2559−2569

this alone would not explain the markedly different Lorentzian line widths observed for features with similar intrinsic oscillator strength in the CH stretch fundamental region.

In previous work on IR excitation of *syn*-CH_3CHOO in the $2\nu_{CH}$ and $\nu_{CH} + \nu_i$ energy regions (ca. 6000 and 4000 cm^{-1}, respectively),[20−22] Lorentzian line broadening was related to the time scale for IVR following excitation of a particular vibrational mode, which occurred on a several picosecond time scale. Within each energy region, the many observed spectroscopic features exhibit similar Lorentzian line broadenings. The spectroscopic features in the $\nu_{CH} + \nu_i$ region exhibit a smaller Lorentzian line broadening and corresponding longer IVR lifetime as compared to the features in the $2\nu_{CH}$ region, which is consistent with a lower density of states in the lower-energy region.

IVR is generally considered to be a tiered process; following IR excitation of a particular spectroscopically bright vibrational state, there is an initial energy transfer to a subset of nearby doorway states that are strongly coupled to this bright state. From this subset of strongly coupled doorway states, energy can then flow into a group of states that are more weakly coupled to the bright state, and so on through successive tiers of states, until the entire manifold of states in the nearby energy range is accessed and IVR is complete.[57]

In this work, we excite vibrational transitions at significantly lower energy. As shown in Figure S3, the density of states in this energy region is extremely low (ca. 5 states/cm^{-1}) and is on the order of the threshold vibrational state density for IVR.[58,59] As a result, there are only a few near-resonant dark states for any given bright state. Most of these states involve the low-frequency HCCO torsional mode (ν_{18}, hereafter referred to as ν_{tor}). As described in Supporting Information, we calculate the torsional energy levels and find that a harmonic approximation of the torsional frequency is fairly good near the bottom of the torsional well. The torsional energy levels are given in Table S5.

Further, in order for the first tier of IVR to occur, the bright state must have significant coupling to a subset of these dark states that are close in energy to the bright state. We therefore look for specific couplings between the broadened carbonyl oxide CH stretch (ν_1) and methyl in-plane CH stretch (ν_2) and near-degenerate dark states, which could promote the initial tier of IVR and lead to the significant Lorentzian line broadening observed for these features. We focus on states with two quanta in CH bends or wags that involve the same CH bond as the stretch of interest. This choice is motivated by the importance of 2:1 bend/stretch Fermi resonances involving CH stretching vibrations.[60,61] We are especially interested in states involving the ν_{tor}, as torsional modes are known to accelerate IVR.[62] With these criteria in mind, we identify the $\nu_5 + \nu_{14} + \nu_{tor}$ combination state as one that is close in energy to ν_2. As ν_5 and ν_{14} are the symmetric and asymmetric methyl scissors, they satisfy the two quanta in the bend criterion. On the basis of VPT2 calculations, the energy difference between these two states is 6 cm^{-1}. We use VPT2 to calculate the off-diagonal coupling between these two states and obtain a coupling matrix element of −23.6 cm^{-1}. This excited state that contains three quanta of excitation is not included in the VPT2 calculation as implemented in Gaussian, and as a result, the energy and coupling are obtained outside of that code using the approaches described in the Supporting Information.

There is a second state with three quanta, $\nu_4 + \nu_{14} + \nu_{tor}$, which is calculated to be 9 cm^{-1} lower in energy than the fundamental in the carbonyl oxide CH stretch (ν_1). This state involves excitation in the CO stretch (ν_4) as well as the asymmetric methyl scissor (ν_{14}) and does not reflect two quanta in bending motions of the carbonyl oxide CH. As a result, the coupling between the carbonyl oxide CH stretch (ν_1) fundamental and this combination state ($\nu_4 + \nu_{14} + \nu_{tor}$) is expected to be weaker, and indeed, it is calculated to be −7 cm^{-1} or approximately a third of the coupling involving the ν_2 fundamental.

In addition, there are anharmonic couplings between the two fundamentals and between the two combination states, which are larger than the couplings between each fundamental and its nearby combination state (see Table S10). A schematic representation of the couplings is shown in Figure S4. As discussed above, the matrix element that couples the methyl in-plane CH stretch (ν_2) fundamental to its nearby combination state ($\nu_5 + \nu_{14} + \nu_{tor}$) is larger than the one that couples the carbonyl oxide CH stretch (ν_1) fundamental to its nearby combination state ($\nu_4 + \nu_{14} + \nu_{tor}$). However, analysis of the four-state system, including all of the off-diagonal couplings in Table S10, shows that both ν_1 and ν_2 gain dark-state character. This analysis is consistent with the broader Lorentzian line widths observed experimentally for the ν_1 and ν_2 features relative to other features in the IR action spectrum in this region.

4.2. Unimolecular Reaction Dynamics. Importantly, IVR is necessary in order for unimolecular decay to OH products to occur following IR excitation. Previous theoretical analysis suggests that four vibrational modes are most relevant in the hydrogen transfer reaction leading to OH: the two out-of-plane CH stretches (ν_3 and ν_{13}), the HCCOO ring-closing mode (ν_{12}), and methyl torsion (ν_{tor}).[19] In order for unimolecular reaction to occur, anharmonic couplings must exist between the vibrational states accessed via IR excitation and the modes involved in the reaction coordinate. This group measured OH appearance rates following IR excitation of $2\nu_{CH}$ (ca. 6000 cm^{-1}) and $\nu_{CH} + \nu_i$ (ca. 4000 cm^{-1}) and found that experimentally measured rates agreed well with RRKM rates including tunneling. No mode-specific effects were observed. This indicates that a statistical distribution of near-resonant vibrational states is achieved on a significantly faster time scale than the unimolecular reaction, which occurs on a few nanoseconds time scale following $2\nu_{CH}$ excitation and on a hundreds of nanoseconds time scale following $\nu_{CH} + \nu_i$ excitation.

We calculate statistical energy-dependent RRKM rates $k(E)$ incorporating quantum mechanical tunneling via semiclassical transition state theory (SCTST) for the 1,4 H atom transfer reaction from *syn*-CH_3CHOO to VHP in the CH stretch fundamental energy region (2850−3150 cm^{-1}). The rates are given in Figure S5 and Table S6. The unimolecular reaction rates in this energy regime are predicted to be slow ($k(E) \approx (1-2) \times 10^5$ s^{-1}). As shown in Figure S3, the density of states of the *syn*-CH_3CHOO Criegee intermediate is quite low (ca. 5 states/cm^{-1}) and on the order of the threshold vibrational state density (∼10 states/cm^{-1}) required for extensive population relaxation by IVR under jet-cooled conditions.[58,59] (By contrast, a Boltzmann distribution under atmospheric conditions will not be subject to the initial state selectivity arising from IR activation.) RRKM theory relies on a statistical population of all vibrational states, which is achieved through fast and complete IVR. With such a sparse density of states, it is possible that IVR of *syn*-CH_3CHOO is incomplete and that

DOI: 10.1021/acs.jpca.8b12324
J. Phys. Chem. A 2019, 123, 2559−2569

the unimolecular decay rates in this energy regime may differ from RRKM theory. With incomplete IVR, mode-specific effects may occur in the unimolecular decay rates, which could increase or decrease the rate depending on the initial coupling between optically bright and dark states and subsequent coupling to modes that promote reaction. That said, the appearance of OH products demonstrates that there is some degree of intramolecular energy redistribution from the initially excited CH stretches to the modes that evolve into the reaction coordinate.

The OH appearance rate impacts the observed intensity of spectral features in the IR action spectrum of *syn*-CH_3CHOO. We have shown previously that the temporal profile of the OH products can be modeled by a dual exponential function, $F(t) = A(-\exp(-(k_{rise} + k_{fall})t) + \exp(-k_{fall}t))$. The exponential rise comes from the unimolecular decay of Criegee intermediates, while the fall is a purely experimental factor that arises from *syn*-CH_3CHOO and OH moving out of the probe region. The exponential falloff occurs on a 1−2 μs time scale. An exponential rise time that is significantly longer than the exponential fall time will significantly decrease the intensity of features observed at a fixed IR-UV time delay, because IR-activated *syn*-CH_3CHOO will move out of the probe region before undergoing unimolecular decay to OH products. For example, at a rise time of 10 μs and a typical experimental fall time of 1.5 μs, only ca. 5% of the intrinsic intensity of a given IR transition will be observed in the IR action spectrum at the peak of its OH appearance time profile. This reduction in peak intensity is illustrated in Figure S6 for a series of simulated rise times.

When the OH rise time is longer (e.g., greater than 2 μs) than the experimental fall time, it is not possible to quantitatively measure the *syn*-CH_3CHOO unimolecular decay rate. In this limit, OH appearance time profiles will be very similar for a variety of slow OH appearance times (see Figure S6). Thus, we place a lower limit of 2 μs for the OH appearance time following IR excitation of *syn*-CH_3CHOO at ca. 3000 cm^{-1}.

The observed experimental intensity also gives qualitative information about the OH appearance rates. Theoretical intensities of CH stretch fundamentals are predicted to be approximately an order of magnitude stronger than those for overtones or combination bands. The experimental intensities observed for the CH stretch fundamental transitions at a fixed IR-UV time delay of 1200 ns (near the peak of the OH appearance time profile) are similar in magnitude to those observed following excitation of combination bands or overtones under the same experimental conditions and near the peaks of their OH appearance time profiles (ca. 500 and 100 ns, respectively). The significant decrease in the observed OH signal following CH stretch fundamental excitation relative to the theoretically predicted transition strength is consistent with a slow (2 μs or slower) time scale for unimolecular decay to OH products.

4.3. OH Orbital Alignment. An intrinsic reaction coordinate (IRC) has been computed at the B2PLYPD3/cc-pVTZ level of theory to obtain insight on the structural changes that occur along the reaction pathway for 1,4 H atom transfer of *syn*-CH_3CHOO, starting from the five-membered cyclic TS to the VHP (H_2C═CHOOH) intermediate, which is formed prior to OO bond fission and dissociation to OH (see Figure 1). Representative geometric structures along the pathway shown in Figure 7 reveal a dramatic change in the

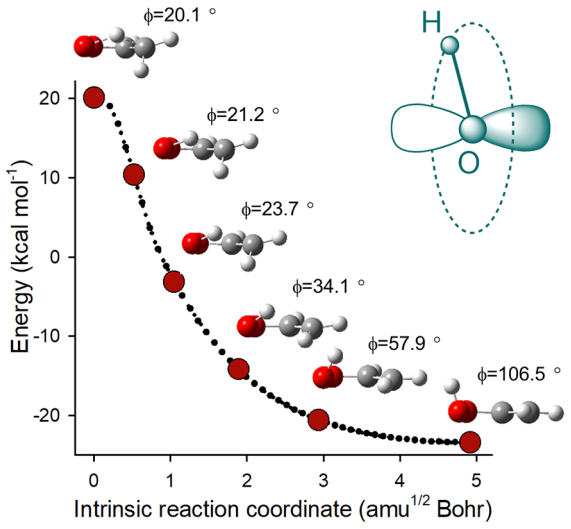

Figure 7. IRC computed for 1,4 H atom transfer of *syn*-CH_3CHOO, starting from its five-membered cyclic TS, to the VHP (H_2C═CHOOH) intermediate prior to dissociation to OH + vinoxy products. The calculations are performed at the B2PLYPD3/cc-pVTZ level of theory without zero-point energy corrections. Representative geometric structures along the path (red points) are shown with ϕ, the angle between the HOO and OOC planes, increasing from an acute (20.1°) to an obtuse angle (106.5°). The resultant torque will induce OH product rotation as the O−O bond breaks. The OH rotation will be orthogonal to the half-filled pπ orbital of the OH radical product (cyan), and results in preferential population of the OH $\Pi(A'')$ λ-doublet levels.

orientation of the transferred hydrogen atom and newly formed OH bond with respect to the OOC heavy-atom plane. At the TS, the newly formed OH bond is tilted only slightly away from the OOC heavy-atom plane. The tilt is defined by an HOOC dihedral angle ϕ between the HOO and OOC planes with ϕ = 20° at the TS. However, the progression of geometric structures along the IRC shows that the OH bond tilts significantly out of the OOC plane to an obtuse HOOC dihedral angle ϕ of greater than 106° for VHP. This geometrical change along the IRC will exert a torque in the plane perpendicular to the O−O bond axis and is expected to induce rotational excitation of the OH radical product as the O−O bond breaks. As a result, the OH fragment rotational motion will be orthogonal to the elongating O−O bond axis, which breaks and results in a half-filled pπ orbital of the OH radical product along this axis.

The degree of electron alignment (DEA) in the OH products,[52,55]

$$\mathrm{DEA} = \frac{\Pi(A'') - \Pi(A')}{\Pi(A'') + \Pi(A')}$$

can be derived from the λ-doublet preference observed experimentally. However, the experimentally derived DEA includes contributions from two sources: (1) dynamical alignment effects and (2) intrinsic electronic wave function mixing effects, $(DEA)_{el}$, the latter of which occur at low-to-moderate N as described in detail elsewhere.[63] Dividing the experimentally derived DEA for each OH product rotational level by $(DEA)_{el}$ yields the reduced DEA, $(DEA)_{red}$, shown in Figure 6 (bottom panel). $(DEA)_{red}$ = −1 indicates that the unpaired pπ orbital is completely aligned perpendicular to the OH rotation plane, $(DEA)_{red}$ = 0 implies no alignment, and

DOI: 10.1021/acs.jpca.8b12324
J. Phys. Chem. A 2019, 123, 2559−2569

$(DEA)_{red}$ = +1 shows that the unpaired pπ orbital is fully aligned in the OH rotation plane.

The OH $X^2\Pi_{3/2}$ (v = 0, N = 2−4) product rotational states observed upon unimolecular decay of IR activated *syn*-CH_3CHOO show a significant degree of pπ orbital alignment perpendicular to the OH rotation plane. IR excitation in the CH fundamental (ν_{CH}), combination ($\nu_{CH}+\nu_i$), and overtone ($2\nu_{CH}$) regions yield similar pπ orbital alignments. In each case, the pπ orbital alignment is greatest for the most populated N = 2 level with $(DEA)_{red} \approx -1$, and decreases as the population drops off toward higher N as shown in Figure 6 (bottom panel).

The observed pπ orbital alignment perpendicular to the OH rotation plane is consistent with the computed IRC: The newly formed OH bond of VHP is moving out of the OOC heavy atom plane, while rapid O−O bond breakage results in the half-filled pπ orbital of OH in the heavy-atom plane. The strong pπ orbital alignment observed perpendicular to the OH rotation plane demonstrates that the VHP intermediate, although transient, plays an important role in the unimolecular decay of *syn*-CH_3CHOO to OH products.

5. CONCLUSIONS

Infrared activation of *syn*-CH_3CHOO in the CH stretch fundamental region (2850 to 3150 cm^{-1}) at energies ca. 3000 cm^{-1} below the TS for 1,4 H atom transfer and associated unimolecular decay is shown to lead to OH radical products. The resultant IR action spectrum acquired using UV LIF detection of the OH products reveals all four of the CH stretch fundamentals (ν_1, ν_2, ν_3, ν_{13}) and the CO stretch overtone ($2\nu_4$) predicted to have strong IR transition strengths. The rotational band contours of the features are analyzed to yield band origins and transition types, which are in good accord with theoretical predictions. Distinctly different Lorentzian line broadening is observed for the CH stretch features, indicating that there are mode-specific couplings between the optically bright states and nearby states. Complementary theoretical calculations suggest that cubic and quartic couplings to nearby states are likely involved in this first step of IVR.

The OH $X^2\Pi_{3/2}$ (v = 0, N) product rotational levels populated upon unimolecular decay show a strong λ-doublet preference, indicating a significant degree of pπ orbital alignment perpendicular to the rotation plane of the OH products. Theoretical mapping of the reaction pathway leading to VHP reveals that the OH bond rotates out of the heavy-atom plane prior to O−O bond breakage. Taken together, this is expected to lead to the λ-doublet preference observed experimentally. This shows that the VHP intermediate, while transient, plays an observable role in the unimolecular decay of *syn*-CH_3CHOO.

Statistical RRKM theory predicts slow unimolecular decay rates ($k(E) \approx (1-2) \times 10^5$ s^{-1} or 5−10 μs time scale) for *syn*-CH_3CHOO in the 3000 cm^{-1} energy region. Experimentally, unimolecular decay is too slow to be measured directly,[22,23] but it is estimated to occur on a several microseconds or slower time scale. The sparse density of states in this region (ca. 5 states/cm^{-1}) suggests that IVR may be incomplete and that unimolecular decay rates may exhibit deviations from statistical behavior. Nevertheless, the appearance of OH products demonstrates that the initially prepared CH stretch fundamental and CO stretch overtone states couple to nearby dark states that lead to OH radical products via quantum mechanical tunneling through the TS barrier.

■ ASSOCIATED CONTENT

Supporting Information

The Supporting Information is available free of charge on the ACS Publications website at DOI: 10.1021/acs.jpca.8b12324.

Experimental band contour analyses and power dependence as well as theoretical evaluation of torsional energy levels and off-diagonal coupling terms, prediction of the vibrational frequencies for *syn*-CH_3CHOO and the transition state, examination of anharmonic couplings, calculation of density of states and unimolecular decay rates for *syn*-CH_3CHOO, and mapping of the intrinsic reaction coordinate leading to vinyl hydroperoxide (PDF)

■ AUTHOR INFORMATION

Corresponding Author

*E-mail: milester@sas.upenn.edu.

ORCID

Victoria P. Barber: 0000-0003-4543-4657

Anne B. McCoy: 0000-0001-6851-6634

Marsha I. Lester: 0000-0003-2367-3497

Notes

The authors declare no competing financial interest.

■ ACKNOWLEDGMENTS

This research was supported through the National Science Foundation under Grant No. CHE-1664572 (M.I.L.). Partial support was also provided by CHE-1619660 (A.B.M.). Parts of this work were performed using the Ilahie cluster at the Univ. of Washington, which was purchased using funds from an MRI grant from the National Science Foundation (CHE-1624430).

■ REFERENCES

(1) Harrison, R. M.; Yin, J.; Tilling, R. M.; Cai, X.; Seakins, P. W.; Hopkins, J. R.; Lansley, D. L.; Lewis, A. C.; Hunter, M. C.; Heard, D. E.; et al. Measurement and Modelling of Air Pollution and Atmospheric Chemistry in the U.K. West Midlands Conurbation: Overview of the PUMA Consortium Project. *Sci. Total Environ.* **2006**, *360*, 5−25.

(2) Emmerson, K. M.; Carslaw, N.; Carslaw, D. C.; Lee, J. D.; McFiggans, G.; Bloss, W. J.; Gravestock, T.; Heard, D. E.; Hopkins, J.; Ingham, T.; et al. Free Radical Modelling Studies during the UK TORCH Campaign in Summer 2003. *Atmos. Chem. Phys.* **2007**, *7*, 167−181.

(3) Elshorbany, Y. F.; Kurtenbach, R.; Wiesen, P.; Lissi, E.; Rubio, M.; Villena, G.; Gramsch, E.; Rickard, A. R.; Pilling, M. J.; Kleffmann, J. Oxidation Capacity of the City Air of Santiago, Chile. *Atmos. Chem. Phys.* **2009**, *9*, 2257−2273.

(4) Taatjes, C. A.; Shallcross, D. E.; Percival, C. J. Research Frontiers in the Chemistry of Criegee Intermediates and Tropospheric Ozonolysis. *Phys. Chem. Chem. Phys.* **2014**, *16*, 1704−1718.

(5) Khan, M. A. H.; Percival, C. J.; Caravan, R. L.; Taatjes, C. A.; Shallcross, D. E. Criegee Intermediates and Their Impacts on the Troposphere. *Environ. Sci.: Processes Impacts* **2018**, *20*, 437−453.

(6) Johnson, D.; Marston, G. The Gas-Phase Ozonolysis of Unsaturated Volatile Organic Compounds in the Troposphere. *Chem. Soc. Rev.* **2008**, *37*, 699−716.

(7) Kroll, J. H.; Hanisco, T. F.; Donahue, N. M.; Demerjian, K. L.; Anderson, J. G. Accurate, Direct Measurements of OH Yields from Gas-Phase Ozone-Alkene Reactions using an in situ LIF Instrument. *Geophys. Res. Lett.* **2001**, *28*, 3863−3866.

(8) Donahue, N. M.; Drozd, G. T.; Epstein, S. A.; Presto, A. A.; Kroll, J. H. Adventures in Ozoneland: Down the Rabbit-Hole. *Phys. Chem. Chem. Phys.* **2011**, *13*, 10848−10857.

DOI: 10.1021/acs.jpca.8b12324
J. Phys. Chem. A 2019, 123, 2559−2569

(9) Drozd, G. T.; Kurten, T.; Donahue, N. M.; Lester, M. I. Unimolecular Decay of the Dimethyl-Substituted Criegee Intermediate in Alkene Ozonolysis: Decay Time Scales and the Importance of Tunneling. *J. Phys. Chem. A* **2017**, *121*, 6036−6045.
(10) Mauldin, R. L., III; Berndt, T.; Sipilä, M.; Paasonen, P.; Petäjä, T.; Kim, S.; Kurtén, T.; Stratmann, F.; Kerminen, V. M.; Kulmala, M. A New Atmospherically Relevant Oxidant of Sulphur Dioxide. *Nature* **2012**, *488*, 193−196.
(11) Hakala, J. P.; Donahue, N. M. Pressure-Dependent Criegee Intermediate Stabilization from Alkene Ozonolysis. *J. Phys. Chem. A* **2016**, *120*, 2173−2178.
(12) Chao, W.; Hsieh, J.-T.; Chang, C.-H.; Lin, J. J.-M. Direct Kinetic Measurement of the Reaction of the Simplest Criegee Intermediate with Water Vapor. *Science* **2015**, *347*, 751−754.
(13) Huang, H.-L.; Chao, W.; Lin, J. J.-M. Kinetics of a Criegee Intermediate that would Survive High Humidity and may Oxidize Atmospheric SO_2. *Proc. Natl. Acad. Sci. U. S. A.* **2015**, *112*, 10857.
(14) Lin, L.-C.; Chang, H.-T.; Chang, C.-H.; Chao, W.; Smith, M. C.; Chang, C.-H.; Jr-Min Lin, J.; Takahashi, K. Competition Between H_2O and $(H_2O)_2$ Reactions with CH_2OO/CH_3CHOO. *Phys. Chem. Chem. Phys.* **2016**, *18*, 4557−4568.
(15) Lewis, T. R.; Blitz, M. A.; Heard, D. E.; Seakins, P. W. Direct Evidence for a Substantive Reaction between the Criegee Intermediate, CH_2OO, and the Water Vapour Dimer. *Phys. Chem. Chem. Phys.* **2015**, *17*, 4859−4863.
(16) Mentel, T. F.; Springer, M.; Ehn, M.; Kleist, E.; Pullinen, I.; Kurtén, T.; Rissanen, M.; Wahner, A.; Wildt, J. Formation of Highly Oxidized Multifunctional Compounds: Autoxidation of Peroxy Radicals formed in the Ozonolysis of Alkenes − Deduced from Structure−Product Relationships. *Atmos. Chem. Phys.* **2015**, *15*, 6745−6765.
(17) Percival, C. J.; Welz, O.; Eskola, A. J.; Savee, J. D.; Osborn, D. L.; Topping, D. O.; Lowe, D.; Utembe, S. R.; Bacak, A.; McFiggans, G.; et al. Regional and Global Impacts of Criegee Intermediates on Atmospheric Sulphuric Acid Concentrations and First Steps of Aerosol Formation. *Faraday Discuss.* **2013**, *165*, 45−73.
(18) Vereecken, L.; Francisco, J. S. Theoretical Studies of Atmospheric Reaction Mechanisms in the Troposphere. *Chem. Soc. Rev.* **2012**, *41*, 6259−6293.
(19) Liu, F.; Beames, J. M.; Lester, M. I. Direct Production of OH Radicals upon CH Overtone Activation of $(CH_3)_2COO$ Criegee Intermediates. *J. Chem. Phys.* **2014**, *141*, 234312.
(20) Liu, F.; Beames, J. M.; Petit, A. S.; McCoy, A. B.; Lester, M. I. Infrared-driven Unimolecular Reaction of CH_3CHOO Criegee Intermediates to OH Radical Products. *Science* **2014**, *345*, 1596−1598.
(21) Fang, Y.; Liu, F.; Barber, V. P.; Klippenstein, S. J.; McCoy, A. B.; Lester, M. I. Communication: Real Time Observation of Unimolecular Decay of Criegee Intermediates to OH Radical Products. *J. Chem. Phys.* **2016**, *144*, 061102.
(22) Fang, Y.; Liu, F.; Barber, V. P.; Klippenstein, S. J.; McCoy, A. B.; Lester, M. I. Deep Tunneling in the Unimolecular Decay of CH_3CHOO Criegee Intermediates to OH Radical Products. *J. Chem. Phys.* **2016**, *145*, 234308.
(23) Fang, Y.; Barber, V. P.; Klippenstein, S. J.; McCoy, A. B.; Lester, M. I. Tunneling Effects in the Unimolecular Decay of $(CH_3)_2COO$ Criegee Intermediates to OH Radical Products. *J. Chem. Phys.* **2017**, *146*, 134307.
(24) Vereecken, L.; Novelli, A.; Taraborrelli, D. Unimolecular Decay Strongly Limits the Atmospheric Impact of Criegee Intermediates. *Phys. Chem. Chem. Phys.* **2017**, *19*, 31599−31612.
(25) Nguyen, T. L.; Lee, H.; Matthews, D. A.; McCarthy, M. C.; Stanton, J. F. Stabilization of the Simplest Criegee Intermediate from the Reaction between Ozone and Ethylene: A High-Level Quantum Chemical and Kinetic Analysis of Ozonolysis. *J. Phys. Chem. A* **2015**, *119*, 5524−5533.
(26) Nguyen, T.-N.; Putikam, R.; Lin, M. C. A Novel and Facile Decay Path of Criegee Intermediates by Intramolecular Insertion Reactions via Roaming Transition States. *J. Chem. Phys.* **2015**, *142*, 124312.
(27) Alam, M. S.; Camredon, M.; Rickard, A. R.; Carr, T.; Wyche, K. P.; Hornsby, K. E.; Monks, P. S.; Bloss, W. J. Total Radical Yields from Tropospheric Ethene Ozonolysis. *Phys. Chem. Chem. Phys.* **2011**, *13*, 11002−11015.
(28) Fang, Y.; Liu, F.; Klippenstein, S. J.; Lester, M. I. Direct Observation of Unimolecular Decay of CH_3CH_2CHOO Criegee Intermediates to OH Radical Products. *J. Chem. Phys.* **2016**, *145*, 044312.
(29) Green, A. M.; Barber, V. P.; Fang, Y.; Klippenstein, S. J.; Lester, M. I. Selective Deuteration Illuminates the Importance of Tunneling in the Unimolecular Decay of Criegee Intermediates to Hydroxyl Radical Products. *Proc. Natl. Acad. Sci. U. S. A.* **2017**, *114*, 12372−12377.
(30) Lester, M. I.; Klippenstein, S. J. Unimolecular Decay of Criegee Intermediates to OH Radical Products: Prompt and Thermal Decay Processes. *Acc. Chem. Res.* **2018**, *51*, 978−985.
(31) Barber, V. P.; Pandit, S.; Green, A. M.; Trongsiriwat, N.; Walsh, P. J.; Klippenstein, S. J.; Lester, M. I. Four-Carbon Criegee Intermediate from Isoprene Ozonolysis: Methyl Vinyl Ketone Oxide Synthesis, Infrared Spectrum, and OH Production. *J. Am. Chem. Soc.* **2018**, *140*, 10866−10880.
(32) Nguyen, T. L.; McCaslin, L.; McCarthy, M. C.; Stanton, J. F. Communication: Thermal Unimolecular Decomposition of *Syn*-CH_3CHOO: A Kinetic Study. *J. Chem. Phys.* **2016**, *145*, 131102.
(33) Long, B.; Bao, J. L.; Truhlar, D. G. Atmospheric Chemistry of Criegee Intermediates: Unimolecular Reactions and Reactions with Water. *J. Am. Chem. Soc.* **2016**, *138*, 14409−14422.
(34) Levine, R. D. *Molecular Reaction Dynamics;* Cambridge University Press: New York, 2009.
(35) Beames, J. M.; Liu, F.; Lu, L.; Lester, M. I. UV Spectroscopic Characterization of an Alkyl Substituted Criegee Intermediate CH_3CHOO. *J. Chem. Phys.* **2013**, *138*, 244307.
(36) Guyer, D. R.; Hüwel, L.; Leone, S. R. Single Collision Ion−Molecule Reactions at Thermal Energy: Rotational and Vibrational Distributions from N^++CO→N+CO^+. *J. Chem. Phys.* **1983**, *79*, 1259−1271.
(37) Frisch, M. J.; Trucks, G. W.; Schlegel, H. B.; Scuseria, G. E.; Robb, M. A.; Cheeseman, J. R.; Scalmani, G.; Barone, V.; Petersson, G. A.; Nakatsuji, H.; et al. *Gaussian 16*, Rev. B.01; Gaussian, Inc.: Wallingford, CT, 2016.
(38) Miller, W. H. Semiclassical Limit of Quantum Mechanical Transition State Theory for Nonseparable Systems. *J. Chem. Phys.* **1975**, *62*, 1899−1906.
(39) Miller, W. H. Semi-Classical Theory for Non-separable Systems:. Construction of "Good" Action-angle Variables for Reaction Rate Constants. *Faraday Discuss. Chem. Soc.* **1977**, *62*, 40−46.
(40) Miller, W. H.; Hernandez, R.; Handy, N. C.; Jayatilaka, D.; Willetts, A. Ab initio Calculation of Anharmonic Constants for a Transition State, with Application to Semiclassical Transition State Tunneling Probabilities. *Chem. Phys. Lett.* **1990**, *172*, 62−68.
(41) Hernandez, R.; Miller, W. H. Semiclassical Transition State Theory. A New Perspective. *Chem. Phys. Lett.* **1993**, *214*, 129−136.
(42) Nguyen, T. L.; Stanton, J. F.; Barker, J. R. A Practical Implementation of Semi-Classical Transition State Theory for Polyatomics. *Chem. Phys. Lett.* **2010**, *499*, 9−15.
(43) Nguyen, T. L.; Stanton, J. F.; Barker, J. R. Ab Initio Reaction Rate Constants Computed Using Semiclassical Transition-State Theory: HO + H_2 → H_2O + H and Isotopologues. *J. Phys. Chem. A* **2011**, *115*, 5118−5126.
(44) Barker, J. R.; Nguyen, T. L.; Stanton, J. F.; Aieta, C.; Ceotto, M.; Gabas, F.; Kumar, T. J. D.; Li, C. G. L.; Lohr, L. L.; Maranzana, A.; et al. *MultiWell-2017 Software Suite;* University of Michigan: Ann Arbor, MI, 2017.
(45) Barker, J. R. Multiple-Well, Multiple-Path Unimolecular Reaction Systems. I. MultiWell Computer Program Suite. *Int. J. Chem. Kinet.* **2001**, *33*, 232−245.

DOI: 10.1021/acs.jpca.8b12324
J. Phys. Chem. A 2019, 123, 2559−2569

(46) Barker, J. R. Energy Transfer in Master Equation Simulations: A New Approach. *Int. J. Chem. Kinet.* **2009**, *41*, 748−763.
(47) Baer, T.; Hase, W. L. *Unimolecular Reaction Dynamics Theory and Experiments;* Oxford University Press: New York, 1996.
(48) Kroll, J. H.; Donahue, N. M.; Cee, V. J.; Demerjian, K. L.; Anderson, J. G. Gas-Phase Ozonolysis of Alkenes: Formation of OH from Anti Carbonyl Oxides. *J. Am. Chem. Soc.* **2002**, *124*, 8518−8519.
(49) Nakajima, M.; Endo, Y. Communication: Spectroscopic Characterization of an Alkyl Substituted Criegee intermediate *Syn*-CH_3CHOO Through Pure Rotational Transitions. *J. Chem. Phys.* **2014**, *140*, 011101.
(50) Western, C. M. PGOPHER: A Program for Simulating Rotational, Vibrational and Electronic Spectra. *J. Quant. Spectrosc. Radiat. Transfer* **2017**, *186*, 221−242.
(51) Altkorn, R.; Zare, R. N. Effects of Saturation on Laser-Induced Fluorescence Measurements of Population and Polarization. *Annu. Rev. Phys. Chem.* **1984**, *35*, 265−289.
(52) Andresen, P.; Ondrey, G. S.; Titze, B.; Rothe, E. W. Nuclear and Electron Dynamics in the Photodissociation of Water. *J. Chem. Phys.* **1984**, *80*, 2548−2569.
(53) Alexander, M. H.; Rackham, E. J.; Manolopoulos, D. E. Product Multiplet Branching in the $O(^1D)+H_2\rightarrow OH(^2\Pi)+H$ Reaction. *J. Chem. Phys.* **2004**, *121*, 5221−5235.
(54) Luque, J.; Crosley, D. R. *LIFBASE: Database and Spectral Simulation Program,* 1.5; SRI International Report MP 99-009; SRI International, 1999.
(55) Andresen, P.; Rothe, E. W. Analysis of Chemical Dynamics via Λ doubling: Directed Lobes in Product Molecules and Transition States. *J. Chem. Phys.* **1985**, *82*, 3634−3640.
(56) Alexander, M. H. OH Electron, Where Art Thou? *Nat. Chem.* **2013**, *5*, 253.
(57) Elles, C. G.; Crim, F. F. Connecting Chemical Dynamics in Gases and Liquids. *Annu. Rev. Phys. Chem.* **2006**, *57*, 273−302.
(58) Lehmann, K. K.; Scoles, G.; Pate, B. H. Intramolecular Dynamics from Eigenstate-Resolved Infrared Spectra. *Annu. Rev. Phys. Chem.* **1994**, *45*, 241−274.
(59) Yoo, H. S.; DeWitt, M. J.; Pate, B. H. Vibrational Dynamics of Terminal Acetylenes: I. Comparison of the Intramolecular Vibrational Energy Redistribution Rate of Gases and the Total Relaxation Rate of Dilute Solutions at Room Temperature. *J. Phys. Chem. A* **2004**, *108*, 1348−1364.
(60) Bernath, P. F. *Spectra of Atoms and Molecules,* 2 ed.; Oxford Univeristy Press: New York, 2005.
(61) Dübal, H. R.; Quack, M. Tridiagonal Fermi Resonance Structure in the IR Spectrum of the Excited CH Chromophore in CF_3H. *J. Chem. Phys.* **1984**, *81*, 3779−3791.
(62) Nesbitt, D. J.; Field, R. W. Vibrational Energy Flow in Highly Excited Molecules: Role of Intramolecular Vibrational Redistribution. *J. Phys. Chem.* **1996**, *100*, 12735−12756.
(63) Hossenlopp, J. M.; Anderson, D. T.; Todd, M. W.; Lester, M. I. State-to-State Inelastic Scattering from Vibrationally Activated OH−H_2 Complexes. *J. Chem. Phys.* **1998**, *109*, 10707−10718.

DOI: 10.1021/acs.jpca.8b12324
J. Phys. Chem. A 2019, 123, 2559−2569